



HAL
open science

Asymptotic waveform inversion for unbiased velocity and attenuation measurements: numerical tests and application for Vesuvius lava sample analysis

A. Ribodetti, S. Gaffet, S. Operto, J. Virieux, Ginette Saracco

► To cite this version:

A. Ribodetti, S. Gaffet, S. Operto, J. Virieux, Ginette Saracco. Asymptotic waveform inversion for unbiased velocity and attenuation measurements: numerical tests and application for Vesuvius lava sample analysis. *Geophysical Journal International*, 2004, 158 (1), pp.353-371. 10.1111/j.1365-246X.2004.02245.x . hal-03099156

HAL Id: hal-03099156

<https://hal.science/hal-03099156>

Submitted on 6 Jan 2021

HAL is a multi-disciplinary open access archive for the deposit and dissemination of scientific research documents, whether they are published or not. The documents may come from teaching and research institutions in France or abroad, or from public or private research centers.

L'archive ouverte pluridisciplinaire **HAL**, est destinée au dépôt et à la diffusion de documents scientifiques de niveau recherche, publiés ou non, émanant des établissements d'enseignement et de recherche français ou étrangers, des laboratoires publics ou privés.

Asymptotic waveform inversion for unbiased velocity and attenuation measurements: numerical tests and application for Vesuvius lava sample analysis

A. Ribodetti,¹ S. Gaffet,¹ S. Operto,¹ J. Virieux¹ and G. Saracco²

¹UMR Géosciences Azur 6526 CNRS/UNSA/IRD/UPMC, F-06235 Villefranche-sur-Mer, France. E-mail: ribodetti@obs-vlfr.fr

²CEREGE, Aix-en-Provence, France

Accepted 2004 January 15. Received 2003 December 12; in original form 2003 May 6

SUMMARY

Recovering physical properties such as attenuation and velocity of the Earth's heterogeneities is as important as recovering the shape and the surface reflectivity of the heterogeneities themselves. A reliable estimate of attenuation in the Earth is necessary to improve our knowledge of subsurface physical properties like the degree of fluid saturation. Moreover the attenuation may also be relevant to 'bright spot' studies in reservoir characterization. Within this context, this paper presents applications of asymptotic viscoacoustic waveform inversion to synthetic and ultrasonic laboratory data recorded to characterize the velocity and attenuation of a lava sample collected on the Vesuvius volcano.

The waveform inversion method is based on a combination of ray theory and the Born approximation to linearize the relation between the scattered wavefield and the velocity and attenuation perturbation models. The iterative linearized inverse problem is solved using the classic least-squares criterion. Asymptotic local analysis of the Hessian operator published in a previous paper by Ribodetti *et al.* showed the theoretical uncoupling between the velocity and attenuation parameters.

The method is first applied to realistic and calibrated synthetic data computed using the discrete boundary integral wavenumber method. The reliability of decoupling between the velocity and attenuation parameters during the inversion is confirmed through two case studies corresponding to a local velocity heterogeneity without any associated attenuation perturbation and a local attenuation heterogeneity without any associated velocity perturbation, respectively.

Second, the method is applied to an ultrasonic laboratory data set that was recorded to determine the velocity and attenuation of a tephrite rock sample collected on the Vesuvius volcano. A velocity of 3200 m s⁻¹ and an attenuation factor of 480 were found, which are consistent with the geological nature of the analysed sample.

The numerical tests presented in this paper validate former theoretical development of asymptotic waveform inversion for characterization of viscoacoustic media. Application to ultrasonic data confirms that the proposed method can be used for reliable estimations of the velocity and attenuation properties of rock from laboratory experiments. Comparable methodology can be extended for use with data from multichannel seismic reflection surveys, providing an opportunity to compare results of laboratory and field experiments.

Key words: attenuation, diffraction tomography, lava, ray theory, rheology, ultrasonic seismic data.

1 INTRODUCTION

Seismic waves propagating through the Earth are attenuated by conversion of a fraction of the elastic energy to heat. In seismic studies, attenuation information increases our knowledge of the properties of rock above that obtained from velocities alone. This particularly concerns the characterization and monitoring of hydrocarbon reservoirs (Sheriff 1975) and, more generally, lithological description of the Earth, i.e. the analysis of the physical state and degree of saturation of rocks. In both laboratory and field measurements the accurate estimation of attenuation is difficult because seismic amplitude is strongly affected by numerous mechanisms such as geometrical spreading, reflections

and scattering in addition to intrinsic damping (Sheriff 1975). It is important that these latter effects are accounted for in order to obtain the true intrinsic attenuation.

Different techniques are used in laboratory and field experiments to study the attenuation of acoustic waves propagating through rocks. Toksöz & Johnston (1981) mainly focused on laboratory measurements of field samples. Methods generally used to measure attenuation in the laboratory may be classified into the following categories: (i) free vibration, (ii) forced vibration, (iii) wave propagation and (iv) observation of stress–strain curves (see Toksöz & Johnston 1981, for a review). Laboratory wave propagation techniques for estimation of sample attenuation within the lower ultrasonic frequency range are of particular interest since these techniques can be extended for use with data from field experiments. A migration/inversion method adapted to acquisition of multichannel seismic reflections was developed for 2-D and 3-D acoustic and 2-D elastic media (Jin *et al.* 1992; Lambaré *et al.* 1992; Forgues 1996; Thierry *et al.* 1999a,b). Extensions of the method to the viscoacoustic and viscoelastic cases were developed by Ribodetti *et al.* (1995) and Ribodetti & Virieux (1998) to retrieve the attenuation factor in addition to velocities and density. The viscoacoustic method was finally adapted to laboratory experiments for the characterization of rock properties (Ribodetti *et al.* 2000).

The inversion method is cast in the general framework of least-squares inverse theory (Tarantola 1987). It uses an asymptotic approximation of the Hessian operator in order to formulate the quasi-Newton inversion through analytical expressions (e.g. Jin *et al.* 1992; Thierry *et al.* 1999a). The linearized inversion relies on a local optimization approach based on iterative least-squares minimization of mismatch between observed and computed scattered wavefields. Model perturbations are parametrized by a grid of point diffractors. The forward modelling (i.e. computation of the wavefields scattered by the model perturbations) is solved under the Born approximation. A dynamic ray tracing is computed in the background medium to estimate ray-related parameters (e.g. traveltime amplitude, geometrical amplitude, attenuation, slowness vectors) required to compute the kernel of the Born integral.

By virtue of Huygens's principle, reflections from continuous reflectors are formed by the superposition of diffractions from the scatterers lying on the reflector. Inversely, the image of a continuous reflector is formed by superposition of the individual contributions of each trace recording the reflection from the reflector. Since this approach strongly relies on the point diffractor parametrization it will be referred to in the following as the diffraction tomography method (DTM). Note that, compared with non-linear iterative approaches for which the forward modelling is solved without any linearization, the background medium remains the same over iterations since Green's functions are computed once by dynamic ray tracing in the initial smooth velocity model.

Some unanswered questions remained in the work of Ribodetti *et al.* (2000) concerning the influence of the experimental set-up (e.g. source–receiver geometry, sample rheological properties) on the estimation of viscoacoustic parameters.

The motivation behind this paper is first to verify the reliability of the method to recover the attenuation Q -factor with a realistic and calibrated synthetic test. The experimental set-up used for the synthetic test is comparable with the one used for the ultrasonic experiment presented hereafter. Second, the method is applied to ultrasonic data recorded in a water tank to estimate the velocity and attenuation of a tephrite rock sample collected on the Vesuvius volcano. This application demonstrates that the DTM approach provides a reliable tool for estimating rock properties as suggested by Ribodetti *et al.* (2000).

The theoretical formulation of DTM is outlined in Section 2 of the paper. The reader is referred to Ribodetti *et al.* (2000) for a detailed description of the method.

Section 3 shows the results of the synthetic test. This test provides an illustration of the overall procedure, which includes the pre-processing of the data to extract the observed scattered wavefield, the iterative inversion *sensu stricto* and a post-processing designed to recover the physical properties of the target from the limited bandwidth tomographic images by adding *a priori* information. Results of the synthetic test demonstrate the pertinence of the acquisition geometry used for the subsequent ultrasonic application and confirm that no trade-off exists between the velocity and attenuation parameters. Two cases are investigated corresponding to (i) a heterogeneity with a local variation of attenuation and no associated velocity perturbation, and (ii) a heterogeneity with a local velocity perturbation only.

The Section 4 shows the application of the method to an ultrasonic laboratory data set that was collected to estimate the velocity and attenuation factor of a Vesuvius lava sample. A velocity of 3200 m s⁻¹ and an attenuation factor of 480 are found which are consistent with *in situ* and laboratory measurements obtained for similar solidified lava (Zamora *et al.* 1994; Vanorio *et al.* 2002) and with tomographic models estimated in this area (Lomax *et al.* 2001; Zollo *et al.* 2002a,b).

Future work will measure the velocity and attenuation in rocks using field seismic reflection experiments, and compare the results with those obtained from physically scaled experiments.

2 THEORY OF 2.5-D VISCOACOUSTIC RAY-BORN INVERSION

The velocity and attenuation of a viscoacoustic medium can be recovered using the tomographic algorithm proposed by Ribodetti *et al.* (2000).

The theory is based on the combination of (i) the ray theory, used to compute the asymptotic Green's functions and (ii) the Born approximation, used to linearize the relation between the scattered wavefield and the model made of small perturbations. Introducing Q in a modelling scheme is equivalent to considering velocity as a complex quantity (Chang & McMechan 1996). The complex velocity \tilde{v} is defined by Toksöz & Johnston (1981):

$$\frac{1}{\tilde{v}} = \frac{1}{v} \left(1 + \frac{i}{2Q} \text{sign}(\omega) \right) \quad (1)$$

where v is the velocity, Q is the attenuation factor and ω is the angular frequency. A frequency-domain inversion allows us to set up an analytical kernel for the Born approximation of the asymptotic anelastic solutions used for the forward problem and an approximate analytical kernel for the linearized inversion. Using the first-order Born approximation and the asymptotic Green's functions for a viscoacoustic medium (Ribodetti *et al.* 2000), we obtain:

$$\delta P(\mathbf{s}, \mathbf{r}, \omega) = \mathcal{K}(\omega) \int_{\mathcal{M}} \mathcal{A}(\mathbf{r}, \mathbf{x}, \mathbf{s}) e^{i\omega T(\mathbf{r}, \mathbf{x}, \mathbf{s})} e^{-\alpha(\mathbf{r}, \mathbf{x}, \mathbf{s})|\omega|} \mathbf{K}(\mathbf{x}, \omega) \begin{pmatrix} \delta v(\mathbf{x}) \\ \delta Q(\mathbf{x}) \end{pmatrix} d\mathbf{x} \quad (2)$$

where, for the 2.5-D geometry, the kernel \mathcal{K} is expressed as

$$\mathcal{K}(\omega) = \frac{1}{\sqrt{-i\omega}} \omega^2 \quad (3)$$

following previous authors (Lambaré 1991; Thierry 1997).

The integration domain \mathcal{M} covers the entire set of scattering points denoted by \mathbf{x} . The source and receiver positions are denoted by vectors \mathbf{s} and \mathbf{r} respectively and the wavefield scattered is denoted by δP while the perturbation model is represented by perturbations $(\delta v, \delta Q)$. The total wave amplitude and the total traveltime associated with the ray travelling from \mathbf{s} to \mathbf{x} and from \mathbf{x} to \mathbf{r} are denoted by \mathcal{A} and T . The total attenuation integrated along the ray path is denoted by α (Aki & Richards 1980). The kernel $\mathbf{K}(\mathbf{x}, \omega) = (a + i \text{sign}(\omega)b; c + i \text{sign}(\omega)d)$ is a complex-valued vector (Ribodetti *et al.* 2000), where

$$a = -\frac{2}{v_0^3(\mathbf{x}, \omega)} \left(1 - \frac{1}{4Q_0^2(\mathbf{x}, \omega)}\right), \quad b = -\frac{2}{v_0^3(\mathbf{x}, \omega)Q_0(\mathbf{x}, \omega)}, \quad c = +\frac{1}{2v_0^2(\mathbf{x}, \omega)Q_0^3(\mathbf{x}, \omega)}, \quad d = -\frac{1}{v_0^2(\mathbf{x}, \omega)Q_0^2(\mathbf{x}, \omega)}.$$

The properties of the background medium are parametrized by a smoothly varying velocity v_0 and attenuation Q_0 . Note that detailed expressions of the vector \mathbf{k} depend only on the rheology of the background medium and not on the source–receiver configuration. The linear relationship that describes the forward problem in eq. (2) can be written in compact form as

$$\delta P = \mathcal{G}\mathbf{f}_{\mathcal{M}} \quad \text{where} \quad \mathbf{f}_{\mathcal{M}}(\mathbf{x}) = \begin{pmatrix} \delta v(\mathbf{x}) \\ \delta Q(\mathbf{x}) \end{pmatrix}. \quad (4)$$

Perturbations of the model parameters δv and δQ are obtained by iterative least-squares minimization of the weighted misfit between the observed and computed wavefields using a quasi-Newtonian algorithm (Jin *et al.* 1992; Thierry *et al.* 1999a). The iterative inversion is linear since the background model is kept constant over iterations. The solution of the quasi-Newtonian inversion is given by:

$$\mathbf{f}_{\mathcal{M}} = [\mathcal{G}^\dagger \mathcal{Q} \mathcal{G}]^{-1} \mathcal{Q} \mathcal{G}^\dagger (\delta P_{\text{obs}} - \delta P_{\text{synth}}) \quad (5)$$

where $\mathcal{G}^\dagger \mathcal{Q} \mathcal{G}$ is the Hessian and $\mathcal{Q} \mathcal{G}^\dagger$ is the weighted gradient. δP_{obs} and δP_{synth} are the observed and computed scattered wavefields, the superscript \dagger denotes the adjoint operator. For the first iteration, $\delta P_{\text{synth}} = 0$ since the background model is homogeneous and perturbations are nil. \mathcal{Q} is a weighting of the cost function.

2.1 Final formulae after diagonalization of the Hessian

In eq. (5), the term to be inverted is the Hessian, which is an operator mapping the model space to itself. It represents a huge matrix whose dimension equals the square of the number of scatterers defining the image. The matrix dimension may increase dramatically and make the numerical inversion computationally expensive. The asymptotic and thus local Hessian approximation for the viscoacoustic case was derived by Ribodetti *et al.* (2000) for a single-offset circular acquisition geometry surrounding the target to be imaged. This acquisition geometry will be used in the applications presented hereafter. This single-offset circular acquisition allows us to illuminate a reflector segment twice (i.e. from both sides of the reflector). This double illumination allows the theoretical uncoupling between the velocity and Q parameters. The asymptotic approximation of the Hessian allows its diagonalization and then its inversion. After diagonalization of the Hessian, the model perturbations $\mathbf{f}(\mathbf{x})$ are computed analytically by a weighted diffraction stack of the data misfit $\Delta \delta P(\phi, \omega) = \delta P_{\text{obs}}(\phi, \omega) - \delta P_{\text{synth}}(\phi, \omega)$.

For the specific acquisition geometry considered in this paper, the final formula used to recover the perturbation is:

$$\mathbf{f}(\mathbf{x}) = -\mathbf{R}^{-1} \sum_{\phi} \frac{\Delta \phi}{\mathcal{A}(\phi, \mathbf{x})} \sum_{\omega^+} \Delta \omega \left| \frac{\partial \mathbf{k}}{\partial(\phi, \omega^+)} \right| e^{i\omega^+|\alpha(\phi, \mathbf{x})} \mathcal{R} e \left[\frac{1}{\mathcal{K}(\omega)} \mathbf{K}^\dagger(\mathbf{x}, \omega^+) e^{-i\omega^+ T(\phi, \mathbf{x})} \Delta \delta P(\phi, \omega^+) \right] \quad (6)$$

where \mathbf{R}^{-1} is the inverse of the matrix \mathbf{R} :

$$\mathbf{R} = \mathbf{K}^\dagger \mathbf{K}(\mathbf{x}, \omega) = \mathbf{K}_-^\dagger \mathbf{K}_-(\mathbf{x}) + \mathbf{K}_+^\dagger \mathbf{K}_+(\mathbf{x}) = \begin{pmatrix} 2(a^2 + b^2) & 2(ac + bd) \\ 2(ac + bd) & 2(c^2 + d^2) \end{pmatrix} = 2 \begin{pmatrix} A & B \\ B & C \end{pmatrix}. \quad (7)$$

In eq. (6), ω^+ stands for the positive frequencies. Inversion of the Hessian matrix now reduces to the inversion of a 2×2 symmetric matrix. This matrix is non-singular, which theoretically proves the uncoupling between the velocity and Q parameters. This matrix can be diagonalized using an equivalent matrix with conditioning number less than or equal to 1 (Forgues 1996). The pair of parameters (\mathbf{s}, \mathbf{r}) are replaced by the single angular parameter ϕ which fully describes the source and receiver positions on a circle (see the following section for a description of the acquisition geometry). The angular step is denoted by $\Delta \phi$ and the angular frequency step by $\Delta \omega$. The inverse of the Jacobian is $|\partial \mathbf{k} / \partial(\phi, \omega^+)|$ for a transformation of variables $|\partial(\phi, \omega^-) / \partial \mathbf{k}| = |\partial(\phi, \omega^+) / \partial \mathbf{k}|$ (see Ribodetti *et al.* 2000, Appendix A for details).

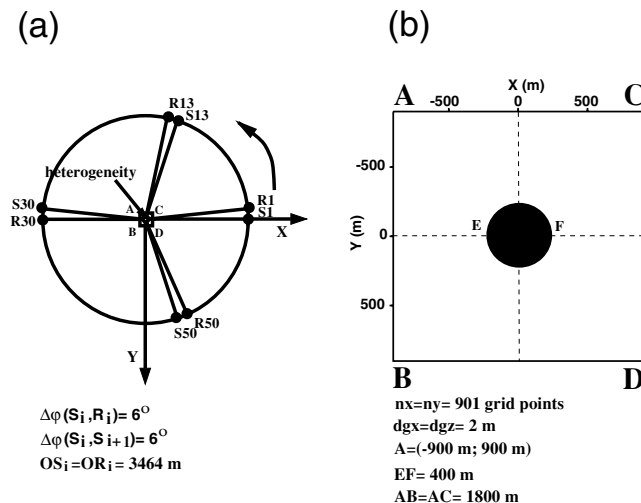


Figure 1. (a) Top view of source–receiver layout. The source and receiver are located in a horizontal plane and turn together around a fixed vertical axis. The offset between the source and receiver is kept constant during acquisition. The heterogeneity is the circular section of cylindrical heterogeneity. The centre of the heterogeneity coincides with the rotation axis of the source–receiver layout. (b) Close-up of the left side centred on the target heterogeneity. The diameter of the heterogeneity is 400 m.

3 NUMERICAL VALIDATION: ACQUISITION GEOMETRY AND NUMERICAL DATA

The method of diffraction tomography is applied hereafter to synthetic data calculated using the discrete wavenumber boundary integral equation method in the viscoelastic case (Gaffet & Bouchon 1989; Gaffet 1995). A fixed-offset experiment is simulated with a circular acquisition geometry providing a complete angular coverage of the target. The target to be recovered by DTM is the circular section of a cylindrical heterogeneity. The source and receiver configuration is depicted in Fig. 1(a). The source and receiver are located on a horizontal plane (X, Y) and rotate together around a fixed vertical axis. The radius of the circle followed by the source and receiver trajectories is 3464 m (i.e. $2s \times v_0$). Offset between source and receiver is kept constant during acquisition (fixed-offset acquisition) with an angle $\Delta\varphi(s_i, r_i)$ of 6° between source and receiver radius. The initial angle ϕ is 0° . The angular step $\Delta\varphi(s_i, s_{i+1})$ between two consecutive source positions is 6° . Sixty seismograms per common-offset gather were computed. The source excitation is an explosion with a Ricker wavelet time dependence in displacement $f(t) = (b - 0.5) \exp^{-b}$ with $b = [\pi(t - t_s)/t_p]^2$, where t_s and t_p are the time of the maximum amplitude and the period of the pulse respectively (Gaffet & Bouchon 1989). The dominant frequency of the synthetic seismograms is 8 Hz. This corresponds to a wavelength of ≈ 200 m in the homogeneous background medium where the velocity $v_0 = 1732$ m s $^{-1}$ and attenuation $Q_0 = 1000$. The diameter of the circular target is 400 m (Fig. 1b). The centre of the disc coincides with the axis of the source–receiver rotating system (Fig. 1a). The target zone $ABCD$ displayed in Fig. 1(b) is discretized with a uniform Cartesian mesh using a grid interval of $dx = dy = 2$ m. The viscoacoustic inversion scheme implies that we can only consider the compressional wavefield using the following relation:

$$\delta P = -(\rho_0 v_0^2) \operatorname{div} \mathbf{u}, \quad (8)$$

where P is pressure, ρ_0 the background density, v_0 the background velocity, and div is the divergence operator applied to the simulated displacement vector \mathbf{u} . Two models are analysed: (i) an attenuation perturbation without velocity variation within the disc denoted by the model $(\delta Q, 0)$ and (ii) a local velocity perturbation without any attenuation variation within the disc denoted by the model $(0, \delta v)$. The perturbation used within the disc is -10 per cent of the reference background model for Q_0 and v_0 . These small amplitude perturbations are consistent with the Born approximation that requires small and local perturbations. The main arrivals in seismograms are coloured in Fig. 2.

3.1 Inversion results

Ribodetti *et al.* (2000) applied the viscoacoustic inversion method to ultrasonic laboratory data and compared the results with rheologies given in the literature. Nevertheless, some questions remain regarding the validity of the estimated parameters. Validation of the DTM inversion requires an accurate control of the source–receiver positions together with an *a priori* knowledge of the rheological properties of the experimental material to be imaged. To achieve this objective and analyse the decoupling of the Q -factor and the velocity, we apply the viscoacoustic inversion method to synthetic data computed in the medium described in the previous section. The numerical data simulated using the discrete wavenumber boundary integral equation method (Gaffet & Bouchon 1989; Gaffet 1995) are hereafter called the *original data*. The attenuation was implemented in the discrete wavenumber boundary integral equation method using the same complex velocity formulation that the one used in the ray–Born formalism, eq. (1). The data computed during the ray–Born inversion are called the *retrieved data*. The model used to generate the *original data* is called the *physical model*. The model constructed using the iterative viscoacoustic inversion process is termed the *tomographic model* or *tomographic image*.

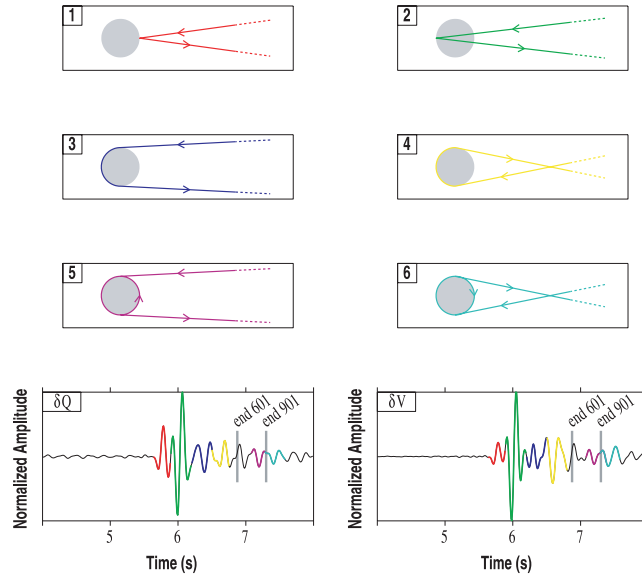


Figure 2. Schematic view of the different traveltimes and arrivals: (1) the red curve represents the first reflected arrival corresponding to the reflection from the surface of the heterogeneity; (2) the green curve represents the secondary arrivals related to the reflection from the inner side of the heterogeneity; (3–6) curves represent different diffracted waves. Seismograms obtained with only local attenuation perturbation and with only local velocity variation are plotted in the lower left and right parts respectively.

The influence of the acquisition system completeness on the decoupling of the attenuation Q -factor and velocity in the *tomographic models* associated with the *physical models* $(\delta Q, 0)$ and $(0, \delta v)$, is analysed using two tests: first, the *physical model* is illuminated with a uniform circular acquisition system. This means that sources and receivers are uniformly distributed along the circle perimeter with a constant spacing between sources and receivers. Second, the same acquisition geometry is considered except that one source–receiver couple is omitted (experiment involving 59 traces instead of 60 in the former case).

The influence of the target zone size $ABCD$ is assessed by comparison of the results obtained from the two following tests corresponding to (i) a large mesh grid around the heterogeneity sampled by 901×901 points and (ii) a smaller mesh grid surrounding the heterogeneity sampled by 601×601 points. In both cases, the mesh interval is the same. Decreasing the grid dimensions is equivalent to considering a narrower time window in the seismograms since shorter scattered ray paths are considered. The objective of this test is to remove from the *original data* later arriving phases such as multiples which are not accounted for by the first-order Born approximation (Fig. 2).

3.1.1 Sensitivity to the completeness of the acquisition system

The inversion was carried out within the frequency range 2–10 Hz corresponding to the source spectra. Ten iterations were computed to obtain the final Q -factor and velocity images for the two studied cases (i.e. $(\delta Q, 0)$ and $(0, \delta v)$). The inversion scheme was stopped short of 10 iterations when the *retrieved data* remain stable and in good agreement with the *original data*. The incomplete data set containing 59 traces was first inverted. The Q -factor and velocity images recovered for the attenuation perturbation model $(\delta Q, 0)$ are displayed in Fig. 3(a). The Q -factor and velocity images obtained for the velocity variation model $(0, \delta v)$ are shown in Fig. 3(b). Although the *tomographic image* includes the source signature implying that both shape and physical dimensions cannot be assessed in a straightforward way, the disc associated with the Q -factor and velocity images is well located and clearly identifiable in Figs 3(a) and (b).

Iterations allow us to update the amplitude of the perturbations, the localization of the *tomographic model* remaining stable all along the iterative process. In Fig. 3 A labels the artefact already observed during the experiment of Ribodetti *et al.* (2000) (see Fig. 8 in Ribodetti *et al.* 2000). It results from the truncation of the source–receiver array resulting from the lack of one source–receiver couple (s_r, r_r) in the acquisition geometry. Fig. 4 related to the complete acquisition geometry (i.e. involving 60 traces) shows that the previous artefact disappears when all source–receiver couples are involved during inversion. Apart from this artefact, the tomographic images are very close in Figs 3 and 4. These tests show the full uncoupling obtained between δQ and δv (compare top and bottom for the *tomographic model* $(\delta Q, 0)$ on Fig. 4(a) and for the *tomographic model* $(0, \delta v)$ on Fig. 4(b)).

3.1.2 Sensitivity to the target size

The shape of the recovered disc tends to become non-circular over iterations (see arrows in Figs 4a and 4b and compare the shape of the heterogeneity at different iterations). This geometrical artefact results from the presence of multiples in the inverted data. Such multiples are not processed properly by the ray–Born single scattering approximation and then would need to be removed from the original data. They

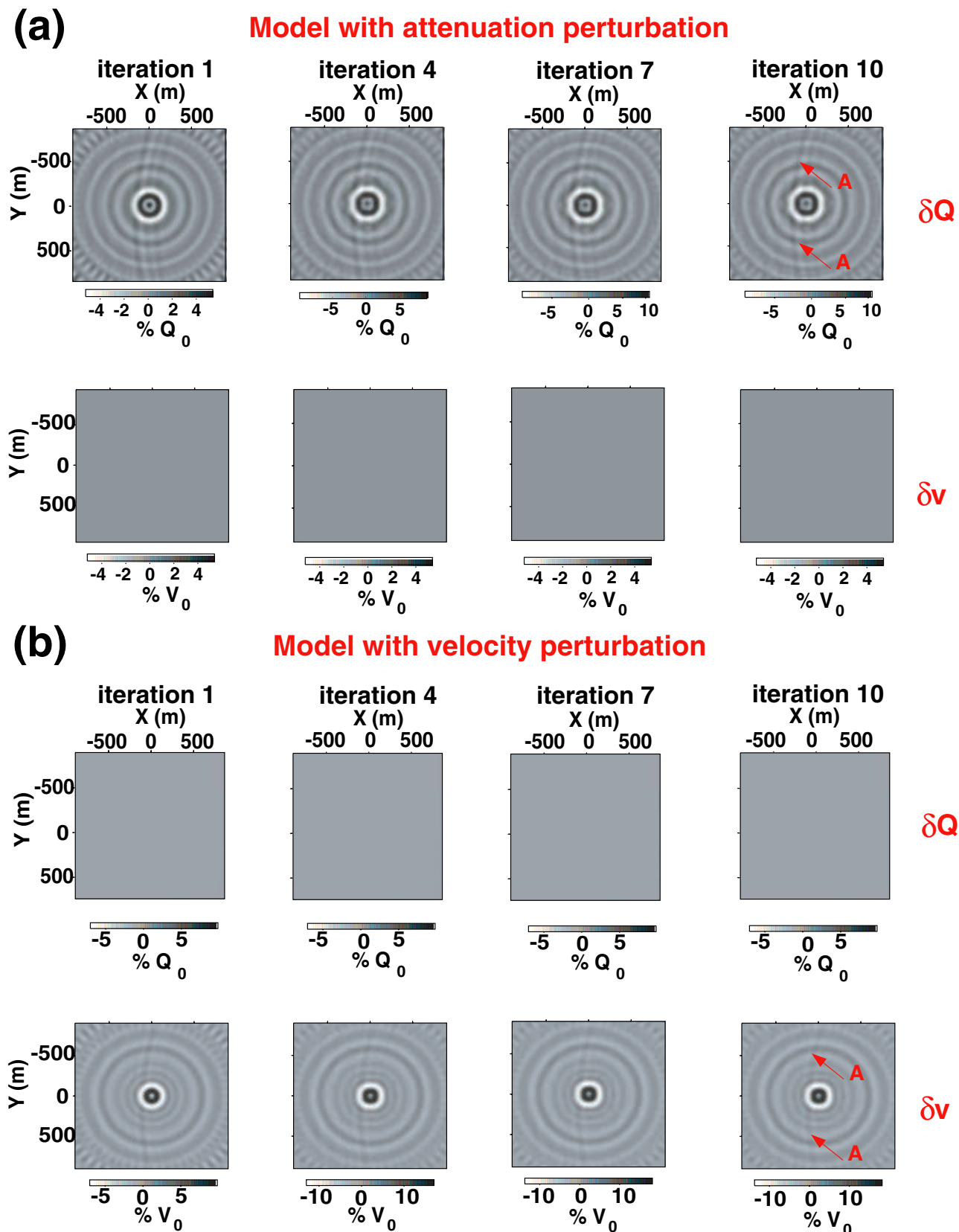


Figure 3. Acquisition of 59 source–receiver couples: (a) model ($\delta Q, 0$): percentage of Q -factor perturbation (upper part) and velocity perturbation (lower part) obtained during iterations 1, 4, 7 and 10—(b) model ($0, \delta v$): percentage of Q -factor perturbation (upper part) and velocity perturbation (lower part) obtained close of iterations 1, 4, 7, and 10. Q and velocity perturbations are fully decoupled in both models. The point A highlights the effect of a missing trace onto the tomographic images. Even if one source–receiver couple is omitted, the tomographic images are well recovered and parameters fully decoupled.

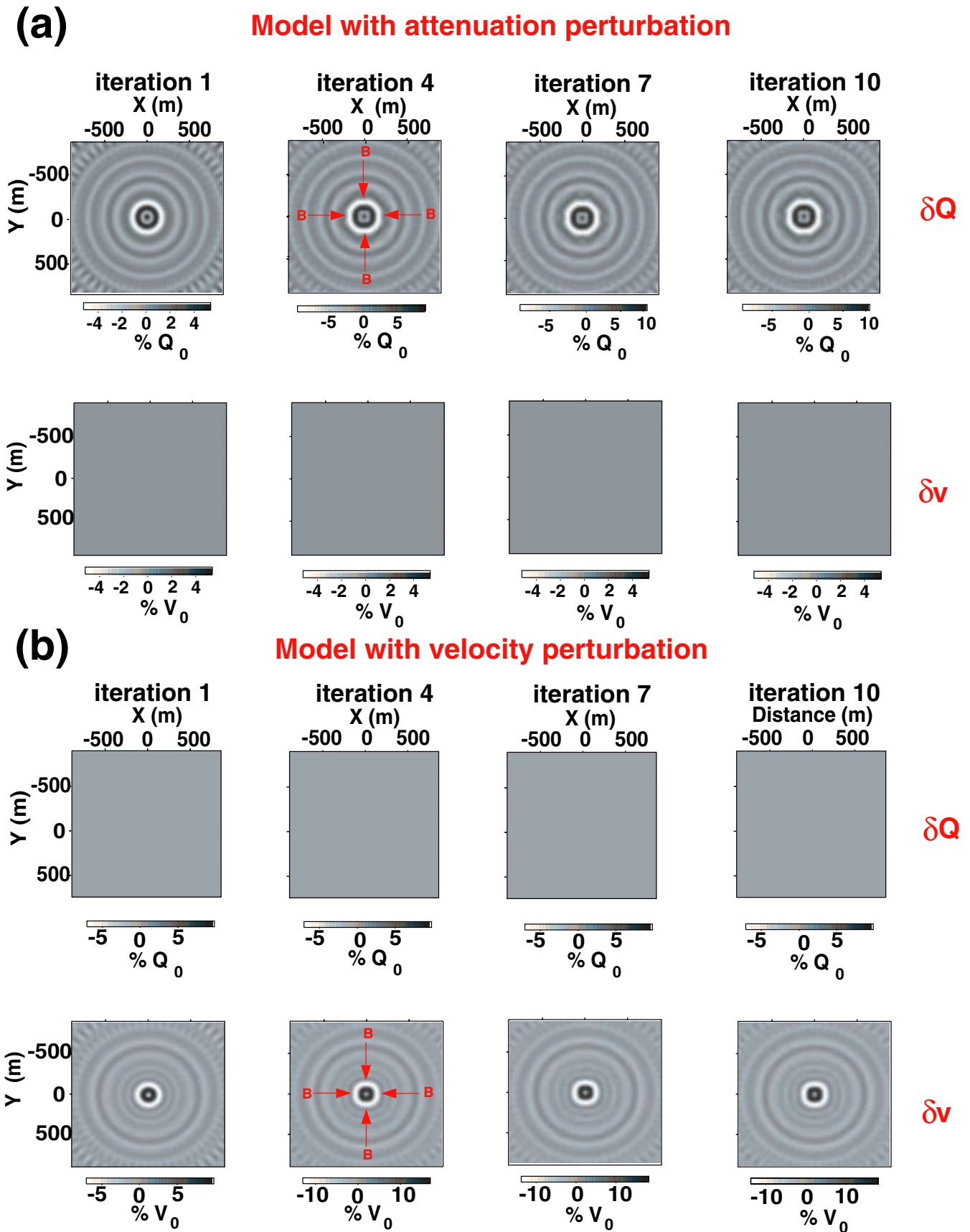


Figure 4. Same as Fig. 3 for the full 60 source–receiver couples configuration. A target of 901×901 points is used.

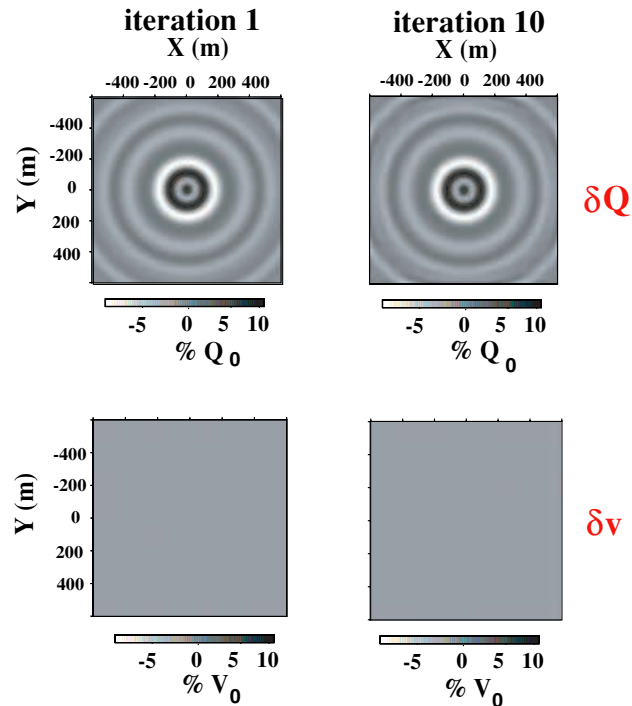
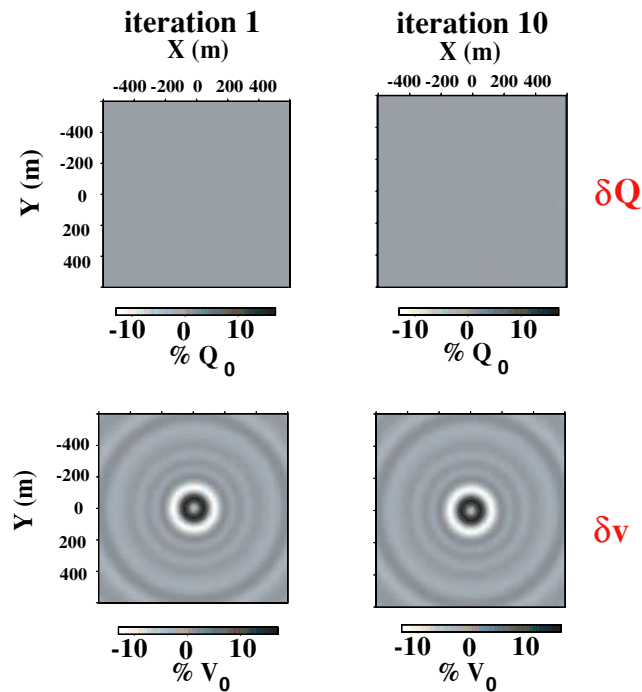
(a) Model with attenuation perturbation**(b) Model with attenuation perturbation**

Figure 5. Same as Fig. 3 for the full 60 source–receiver couples configuration. A target of 601×601 points is used.

correspond to phases labelled 5 and 6 in Fig. 2 around 7 s. These later-arriving phases tend to be stacked constructively over iterations and migrated at the wrong locations. This constructive stack is favoured both by the iterative procedure and the non-redundancy of the single-offset acquisition geometry. This causes the distortion of the target image observed after several inversion iterations in Figs 3 and 4. Note that this kind of distortion is not observed when the forward modelling (i.e. computation of Green's functions) is computed by full waveform methods such as finite differences since they account properly for multiple arrivals (Dessa & Pascal 2003). To remove the footprint of the multiples on the tomographic images, we consider a smaller grid size sampled by 601×601 nodes with the same grid interval (Fig. 5). Such a smaller

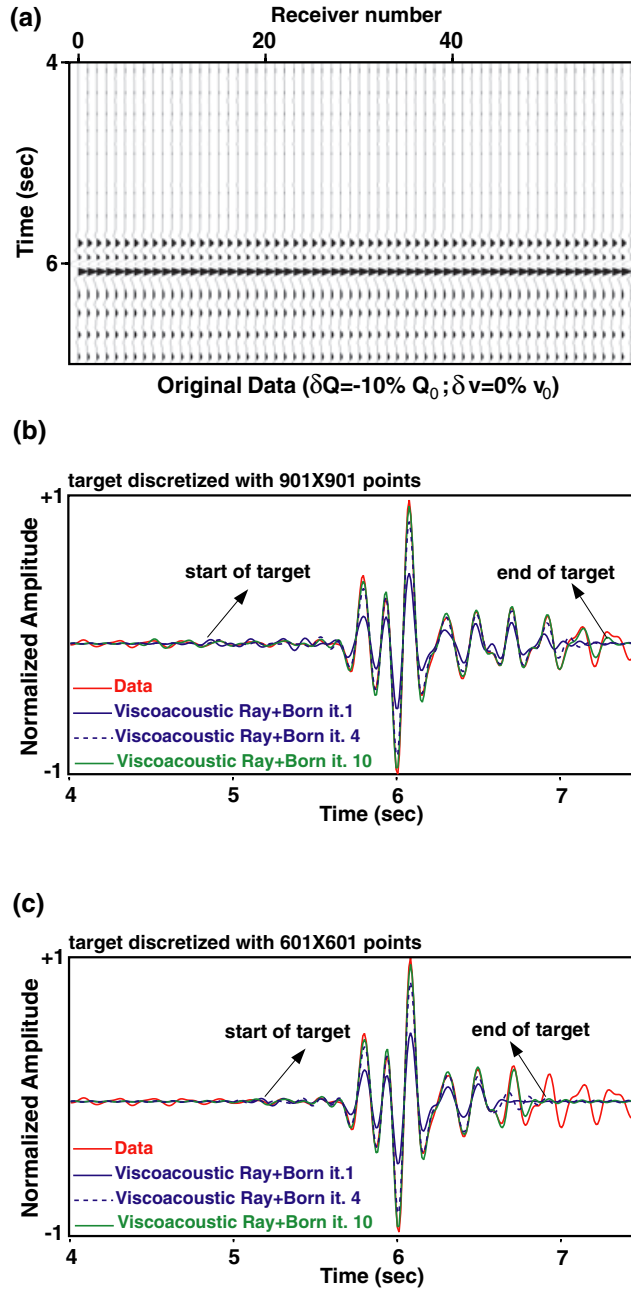


Figure 6. Model $(\delta Q, 0)$: (a) *original data*; (b) target zone of 901×901 points: *original data* (red line) is superimposed with *retrieved viscoacoustic data* at the first, fourth and tenth iterations (respectively blue, dashed blue and green lines). (c) Same presentation for the target zone of 601×601 points.

target zone allows us to narrow the time window in the seismograms such that only the primary reflected phases are involved in the inversion (Fig. 2).

Fig. 5 displays the results obtained using such a smaller target zone of 601×601 points. No geometrical distortion between the first and the last iterations appears now as depicted in Fig. 5. In order to verify the efficiency of the iterative inversion, the *original data* and the ray–Born viscoacoustic *retrieved data* are compared for the two models of Figs 6 and 7. Figs 6(a) and 7(a) present the *original data*. An excellent agreement is obtained close to iteration 10 between *original data* and *retrieved data* as shown in Figs 6b and 6c and Figs 7(b) and (c). At this step of the DTM process, the excellent match between the *original data* and *retrieved data* (Figs 6 and 7) and the full decoupling between δQ and δv (Figs 3, 4 and 5) confirm numerically the results expected from the theoretical development of the Hessian operator which was shown to be non-singular for the circular acquisition geometry (see eq. 7 and Ribodetti *et al.* 2000, for more details).

3.2 Post-processing of images: absolute geometry and analysis of properties of the medium

A deconvolution-like post-processing is designed in order to remove the limited bandwidth source signature from the tomographic Q -factor and velocity images (Fig. 8 box 2 corresponds to Fig. 5 at iteration 10). This procedure allows us finally to estimate the absolute values of the

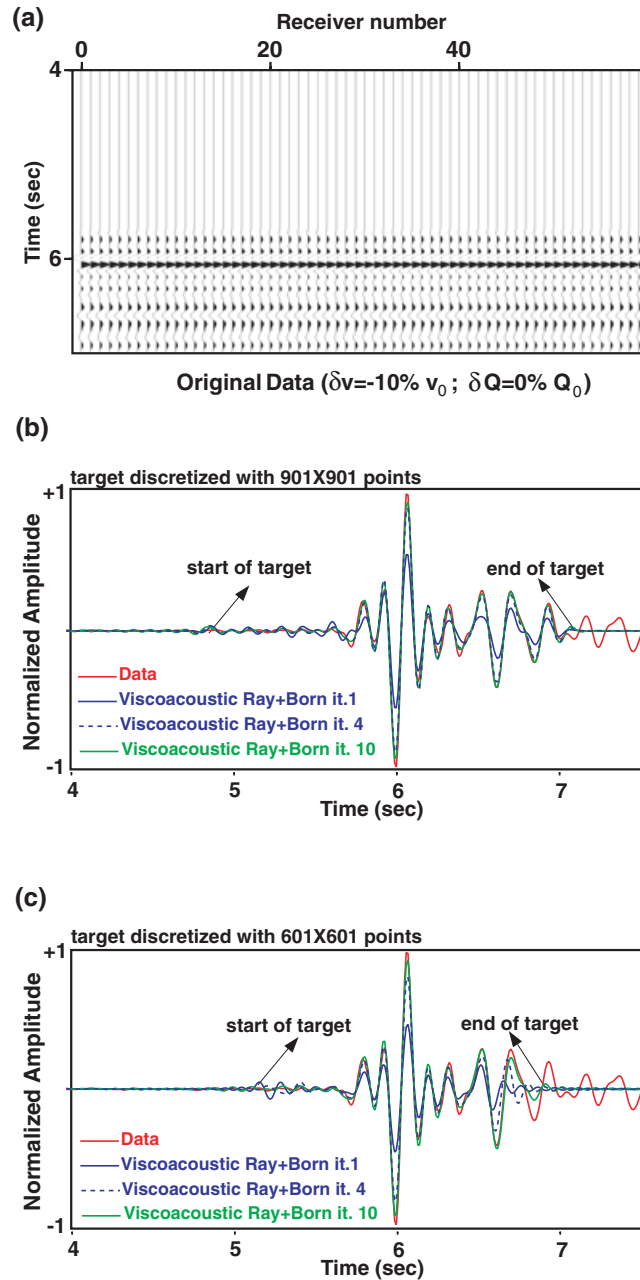


Figure 7. Same as Fig. 6 for the model $(0, \delta v)$.

attenuation Q -factor and velocity in the heterogeneity as shown in Fig. 8 (box 7). The post-processing is formulated as a series of 1-D inverse problems. The data set associated with one inverse problem is a section of the 2-D tomographic image extracted along one azimuth (Fig. 8 box 3). The inverse problem is solved for several closely spaced azimuths ranging from 0° to 360° such that the full 2-D tomographic image is considered in the inversion. By the end, a 2-D synthetic tomographic image is built by assembling all the 1-D sections in the (X, Y) plane (Fig. 8 box 6).

The *model space* is a family of centred boxes (Fig. 8 box 4) with a variable amplitude and width. These boxes mimic the section of the true *physical model* (i.e. the section of the cylinder). The amplitude of the boxes represents the absolute values of attenuation Q -factor and velocity in the cylinder. The width of the boxes represents the thickness of the heterogeneity (i.e. the diameter of the cylinder). The *predicted or synthetic data set* is computed from the boxes through a simple convolution with the source wavelet. The boxes are transformed from perturbation space to time space using the velocity of the background medium and convolved with the source wavelet (Fig. 8 box 5). Then, the convolved box is converted back to perturbation space for comparison with the section extracted from the *tomographic model* (Fig. 8 box 3).

Since the forward problem is a simple convolution, the inverse problem can be solved using a grid search of the parameters. Given one azimuth (Fig. 8 box 3), the log of the tomographic model is compared with each convolved synthetic log (i.e. the box after convolution with the source wavelet) sampling the model space. The best fitting model is determined under the L_2 -misfit criteria. Assemblage of the best fitting

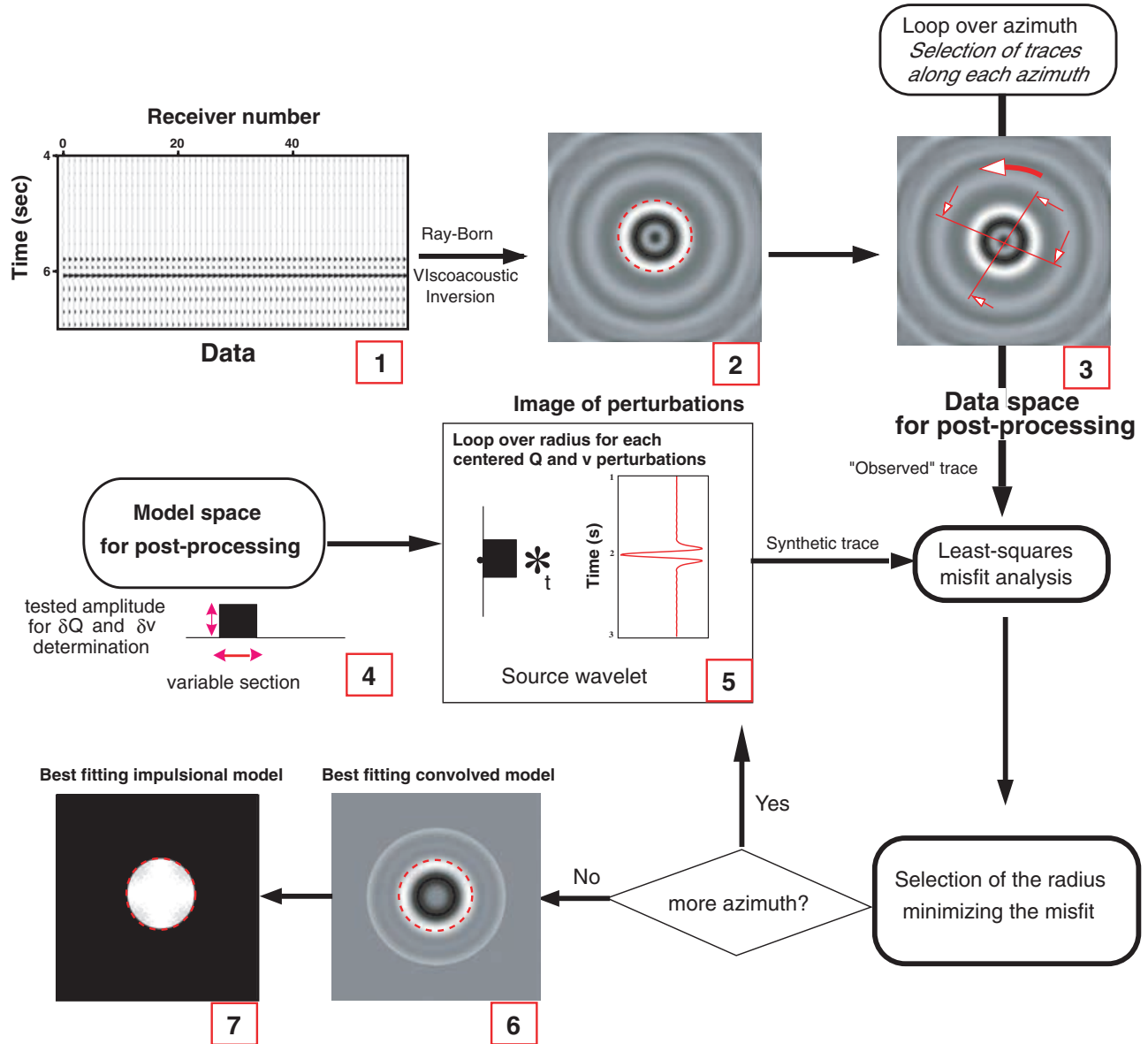


Figure 8. Post-processing scheme allowing both deconvolution of *tomographic images* from the source signature and estimation of the absolute value of attenuation Q -factor and velocity in heterogeneity.

boxes and the associated synthetic logs in the (X, Y) plane allows to verify that the 2-D shape of the heterogeneity was properly recovered by the independent 1-D inverse problems (Figs 8 box 6 and 8 box 7).

The best δQ and δv values corresponding to the minima of the attenuation and velocity misfits are displayed for one azimuth in the upper and lower parts of Fig. 9(b). Forty radii were tested with a step of 10 m. The best fitting values are $\delta Q = -100$ and $\delta v = -173 \text{ m s}^{-1}$ which exactly correspond to the *physical model* perturbations introduced numerically (i.e. -10 per cent for the Q -factor and -10 per cent for velocity). The shape and the dimension of the recovered heterogeneity are in excellent agreement for both the attenuation Q -factor and the velocity *retrieved models* (Figs 9a and c) in comparison with the original *physical model* used to compute the *original data*. The absolute value of the heterogeneous physical properties (i.e. velocity and attenuation factor) can be deduced by simple summation of the homogeneous background medium properties with the estimated model perturbation ones: $v = v_0 + \delta v$ and $Q = Q_0 + \delta Q$.

4 APPLICATION TO ULTRASONIC LABORATORY DATA FOR ESTIMATING PROPERTIES OF LAVA SAMPLES

The objective of this section is to estimate the seismic velocity and attenuation Q -factor of calibrated rock samples using laboratory viscoacoustic diffraction tomography as developed by Ribodetti *et al.* (2000).

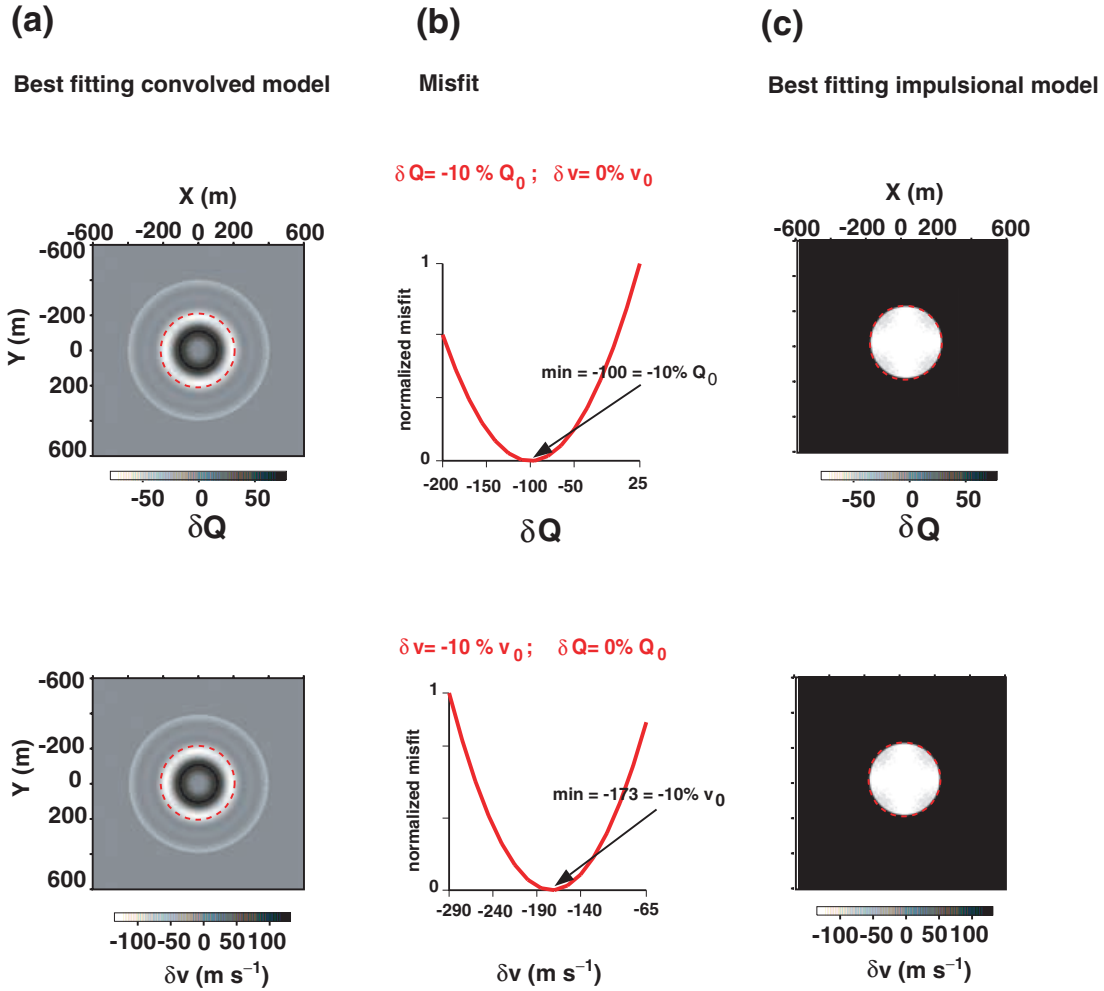


Figure 9. Results of the processing sequence for the attenuation Q -factor (top) and velocity (bottom). (a) Best fitting convolved models for attenuation and velocity perturbations deduced from procedure described in Fig. 8. (b) Misfit between attenuation Q -factor perturbation *tomographic image* and the best fitting convolved model. (c) Dimension and shape of discs δQ and δv are in good agreement with the *original model geometry*.

4.1 Lava sample and experimental set-up

A cylindrical tephrite rock sample (also called ‘black lava’) collected in the quarry of Boscotrecase near to the Vesuvius volcano, Italy, is analysed (Fig. 10). The diameter of the sample is 0.06 m and its height is 0.50 m. As in the experiment performed by Ribodetti *et al.* (2000), the measurement is carried out in a water tank. The water tank located at the University of Rennes (France) measures $2.0 \text{ m} \times 1.40 \text{ m} \times 1.50 \text{ m}$ and includes a computer-based control and data acquisition systems (see Valero 1997, for a more complete description of this experimental apparatus). Five thousand litres of water are used to fill the tank and constitute the constant-velocity background medium. Two hydrophones are used for the source and receiver. The frequency bandwidth of hydrophones ranges between 1 kHz and 70 kHz. The source and receiver configuration are identical to the numerical test presented in the previous section (Fig. 1). The source and receiver are located in a horizontal plane surrounding the sample (Fig. 10). The axis of the sample cylinder corresponds to the axis of the source–receiver rotating system. The radius of the circle described by the source and receiver trajectories is 0.469 m. The offset between source and receiver is kept constant during acquisition (fixed-offset acquisition) with an angle $\Delta\Phi_{\text{sr}}$ of 15° between the source and the receiver radius. The source and receiver hydrophones are 0.67 m below the water surface. The initial angle ϕ is 7.5° . The angular step $\Delta\Phi_s$ between two consecutive source positions is 5° leading to 72 seismograms per common-offset gather. The dominant frequency of signals emitted by the source hydrophone is 40 kHz corresponding to a wavelength of $\approx 0.04 \text{ m}$ in water. Waveforms are recorded with a sampling frequency of $1 \times 10^6 \text{ Hz}$. The source and receiver lie in a common (X, Y) horizontal plane. The target geometry (i.e. the cylindrical shape of the cylinder) is invariable along the Z vertical axis. Such a configuration leads to a 2.5-D geometry where the heterogeneity is a circular section of the lava cylinder located in the horizontal plane defined by the source and receiver positions (Fig. 10). The target zone is sampled using a uniform mesh of 500×500 nodes with a mesh spacing $dx = dy = 0.001 \text{ m}$.

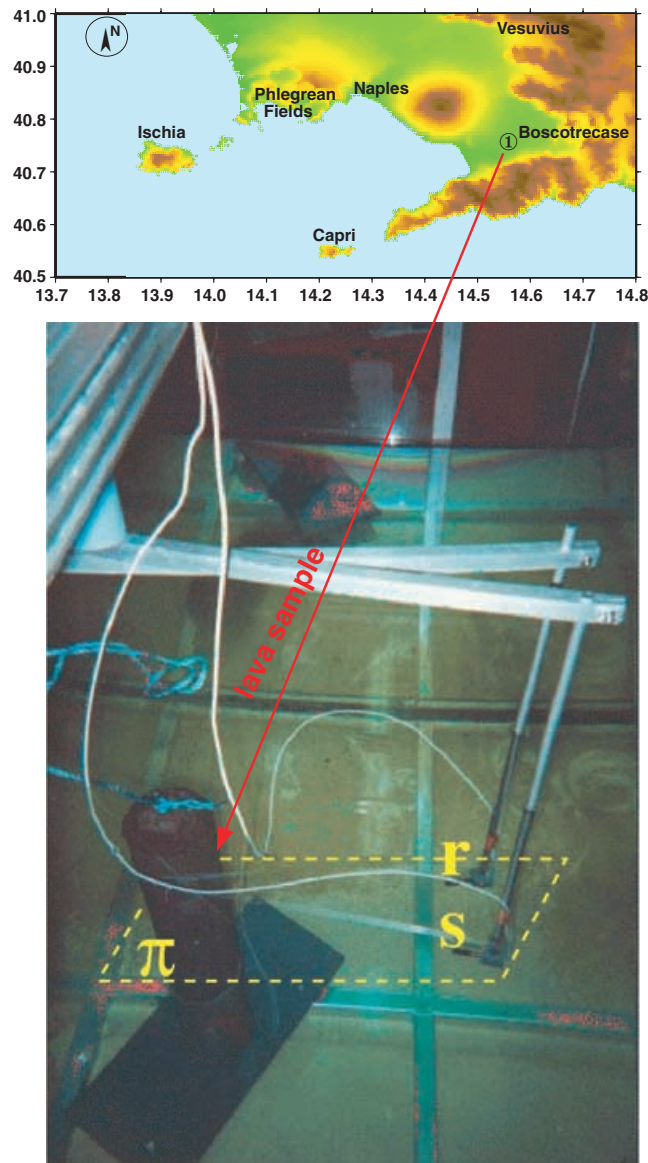


Figure 10. Map of Vesuvius area and water tank with lava sample from Boscotrecase.

4.2 Pre-processing of data and background medium analysis

Only the wavefield diffracted by the lava sample is processed. The scattered wavefield is presented in Fig. 11. The arrival at around 0.63 ms is the reflection from the surface of the lava sample. The recorded data are not aligned along a straight line as in the numerical simulations shown in Figs 6(a) and 7(a) because the cylinder axis does not exactly coincide with the centre of the acquisition circle (Fig. 1a). Data are band-pass filtered within the frequency range 15–55 kHz corresponding to wavelengths of ≈ 0.25 to ≈ 1.0 times the diameter of the lava sample. In the framework of ultrasonic experiments which involve very short wavelengths, an accurate estimation of water velocity is important since the location of the structures in the image is sensitive to the accuracy of the background model (i.e. the accuracy of the estimation of the water velocity). A water velocity $v_0 = 1489 \text{ m s}^{-1}$ and attenuation Q -factor $Q_0 = 210\,000$ corresponding to a temperature of 20° C and mean frequency of 100 kHz (Fujii & Masui 1993; Toksöz & Johnston 1981), are used.

4.3 Inversion results and post-processing of images: geometry and analysis of properties of the medium

Inversion was carried out within the frequency range 33–45 kHz. This scaled experiment uses wavelengths approximately equal to the diameter of the lava sample, as in the simulation detailed in the previous numerical experiment. Five iterations were computed to obtain the final velocity and attenuation Q -factor images. The recovered Q and velocity images are shown in Fig. 12 close to iterations 1, 3 and 5. The shape and dimension of the recovered object are difficult to estimate accurately because the source signature is convolved with the tomographic image. Thus, at this stage, the amplitudes of the perturbation remain relative (i.e. the picture is chosen to be dimensionless) and the absolute values

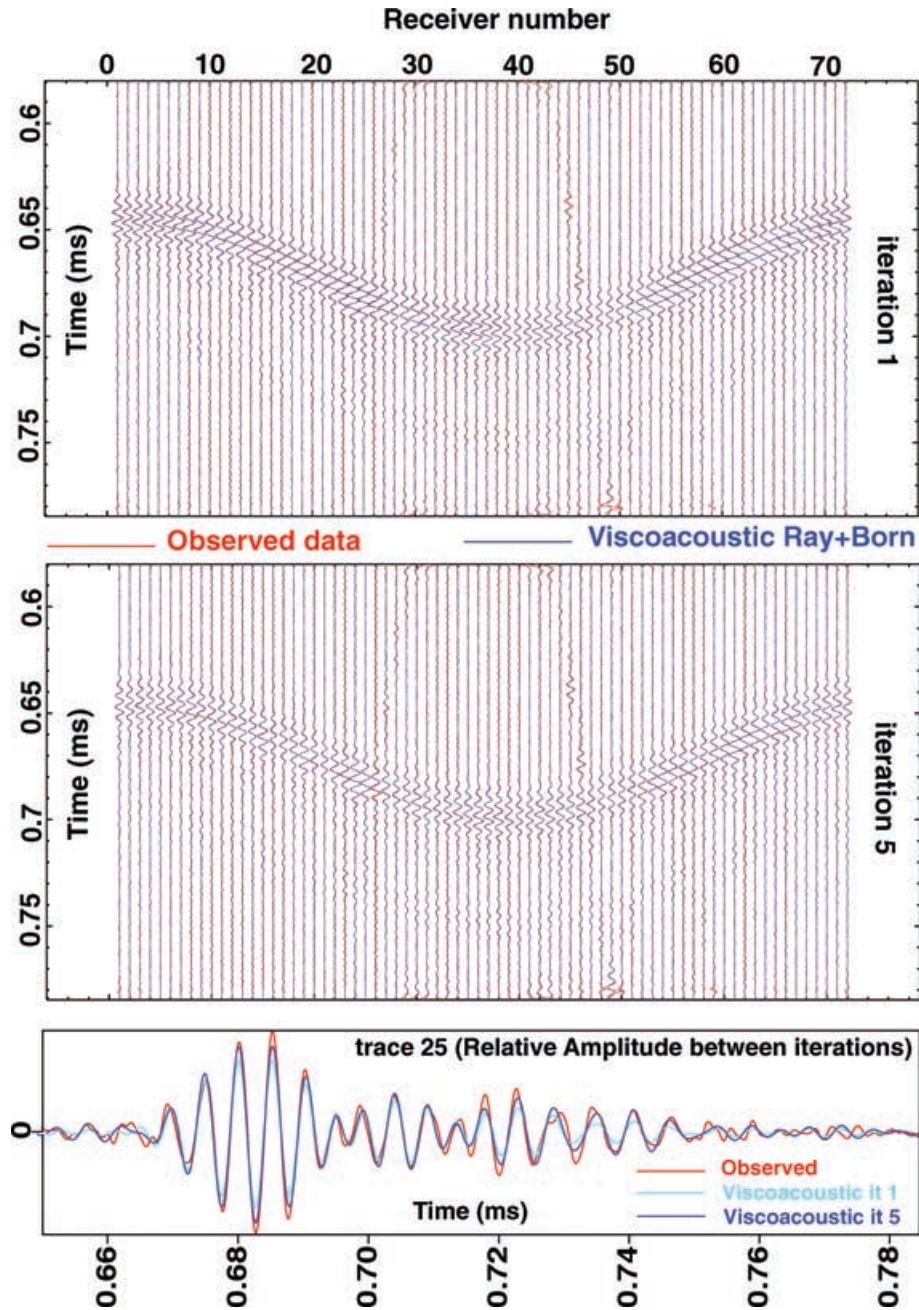


Figure 11. Observed data in red are superimposed with synthetics at the first and fifth iterations. At the bottom of the figure there is a comparison between the observed and the computed trace 25 close to iterations 1 and 5 showing the improvement of the fit over iterations.

of the physical parameters will only be determined in the subsequent post-processing deconvolution. The main effect of iterations is to update the amplitude of perturbations since the shape and location of the object do not vary significantly over iterations.

The overall good continuity of Q and velocity images of the cylinder suggests that the estimation of these two parameters is reliable along most of the cylinder contour. Some local discontinuities in the shape of the Q and velocity tomographic models are labelled A, B, C and A, B respectively in Fig. 12. The discontinuities are probably related to the inaccuracies of the experimental set-up (i.e. noisy traces). In order to check the efficiency of the iterative inversion, the fit between observed data and the ray–Born synthetics, superimposed in Fig. 11, is quantified by the root mean square misfit (rms misfit) over iterations in Fig. 13.

The quality of the fit between observed and predicted seismograms asymptotically increases with the number of iterations. The iterative procedure is stopped when the rms variation is less than 5 per cent of the rms obtained from the previous iteration. Due to the dedicated weighting of the Hessian operator (see eq. 5, Appendix A1 in Ribodetti *et al.* 2000), the first iteration fits the data very well by itself. In practice, as shown in Fig. 13, five iterations are enough to achieve a good fit. Fig. 13 shows the evolution of the rms until the 20th iteration. The

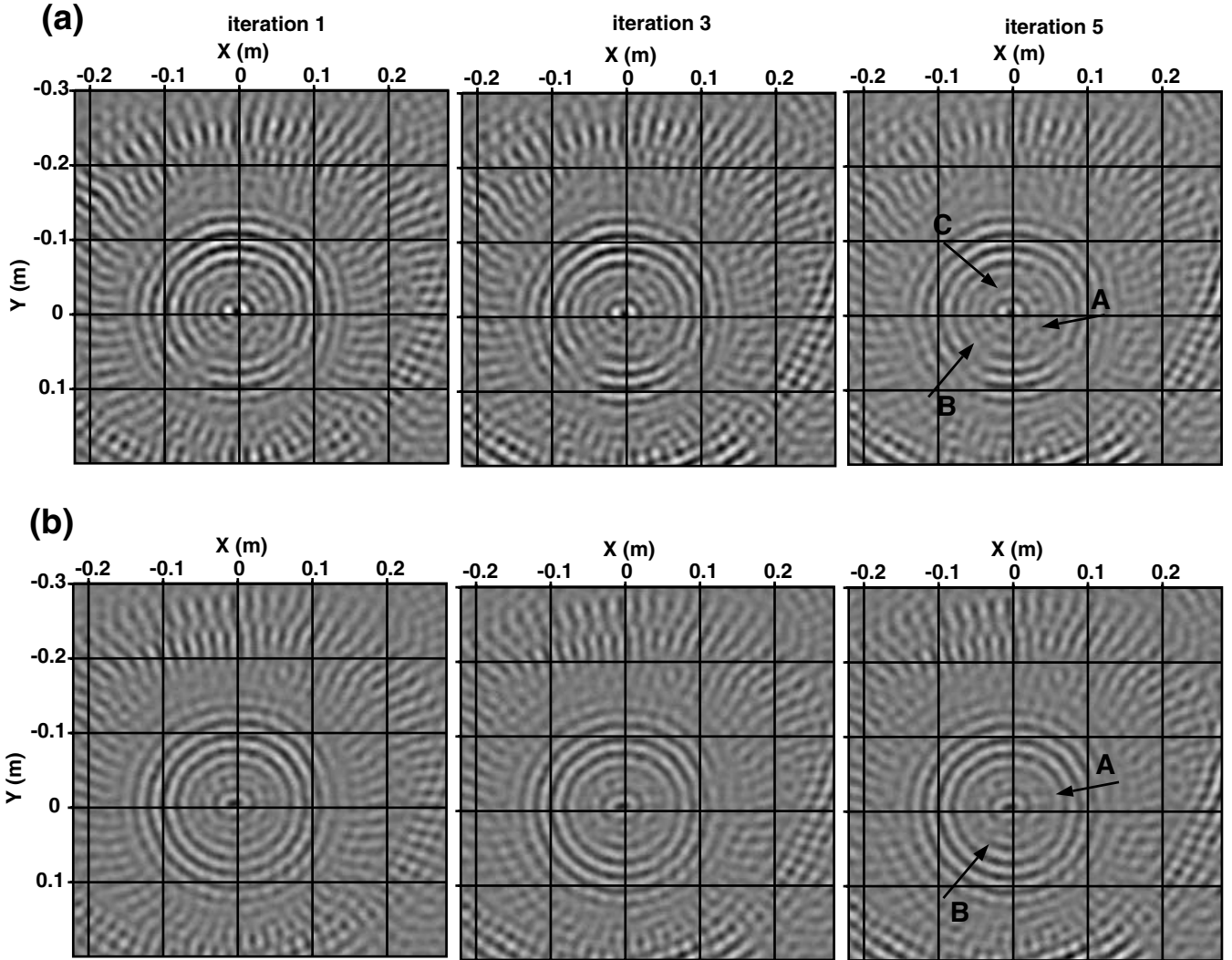


Figure 12. Tomographic models for attenuation (a) and for velocity (b) over iterations.

fit improvement after the fifth iteration is not really significant because at this level of resolution the acquisition noise becomes predominant and cannot be explained by the synthetic simulation. This noise level leads to a rms misfit greater than 0.

The post-processing procedure described in the previous section is applied in order to remove the source signature from the tomographic images and to estimate the absolute value of the attenuation Q -factor and velocity in the cylinder. Results of this post-processing are depicted in Figs 14 and 15 for the attenuation Q -factor and for the velocity perturbations respectively. The source signature was obtained by stacking the direct wave travelling from the source to the receiver (Fig. 14b). The best fitting impulse model representing the absolute value of the Q perturbations within the lava sample and its geometry is presented in Fig. 14(b). An attenuation factor of 480 is obtained within the lava sample (Fig. 14b). A 3-D view of the misfit as a function of azimuths and Q perturbation δQ is presented in Fig. 14(c) to illustrate the robustness of the estimation of Q with respect to the azimuth. The projection of the misfit on the plane (δQ , azimuth) exhibits local minima around $\delta Q = 2.09520 \times 10^5$. For some azimuth (i.e. (1° , 10°) and (160° , 180°)) the minimum of the misfit is mislocated and the attenuation perturbation is overestimated. The same processing sequence is applied to the velocity perturbation tomographic model. A homogeneous velocity around 3200 m s^{-1} was found within the lava sample (Fig. 15b). A 3-D view of the misfit as a function of the azimuths between 0° and 180° and of the tested δv is presented in Fig. 15(c). The level misfit surface shows local minima around $\delta v \approx 3700 \text{ m s}^{-1}$. For some azimuths around 30° and around 150° the minimum of the misfit is obtained for underestimated values of δv (Fig. 15c bottom). The post-processing successfully recovered the shape of the cross-section of the lava sample, although some local discontinuities are observed in the synthetic tomographic images (Figs 14a and 15a) and the impulse models of the lava sample (Figs 14b and 15b). These discontinuities are labelled A, B, C and A, B for the attenuation factor Q and velocity respectively in Figs 14(a) and (b) and in Figs 15(a) and (b). The discontinuities may result from noisy traces in the observed data related to inaccuracies of the acquisition system.

The estimated value of the Q -factor ($Q = 480$) is consistent with the basaltic nature of the lava sample (Toksöz & Johnston 1981, p. 104, $Q = 590$ for basalt) and indicates a more elastic response than a viscous behaviour; the estimated velocity of the tephrite ($v = 3189 \text{ m s}^{-1}$) is

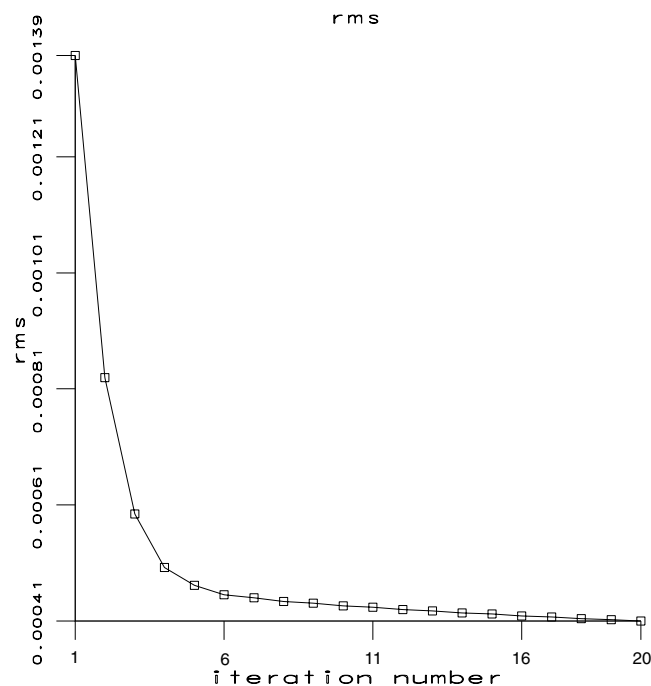


Figure 13. Rms misfit versus iteration number.

quite low; however, it is within the range of velocities obtained from *in situ* and laboratory measurements for similar solidified lava (Zamora *et al.* 1994; Vanorio *et al.* 2002) and from tomographic studies carried out in this area (Lomax *et al.* 2001; Zollo *et al.* 2002a,b).

5 CONCLUSION

The viscoacoustic tomography presented in this paper provides the attenuation Q -factor and velocity of heterogeneities without any trade-off between the two classes of parameters. To verify these theoretical results, asymptotic viscoacoustic diffraction tomography using an iterative quasi-Newtonian formulation was first applied to synthetic data computed using the discrete wavenumber boundary integral equation method. The various tests confirm that the attenuation Q -factor and velocity parameters are fully decoupled for a circular acquisition geometry surrounding the target. Even if one source–receiver couple is omitted in the circular source–receiver array, the method remains stable and the *tomographic model* is well recovered. Both *tomographic models* of the attenuation Q -factor and velocity allow us to clearly characterize the geometry and the rheology of the *physical heterogeneity*. The excellent agreement between *observed data* and viscoacoustic predicted synthetic seismograms demonstrates the validity of the iterative viscoacoustic modelling and inversion steps. A deconvolution-like post-processing of the tomographic image allows us to remove the source signature from the attenuation factor and velocity tomographic images in order to estimate the absolute values of the velocity and attenuation factor inside the true sample, assuming the spatial distribution of expected heterogeneities. The full process was finally applied to ultrasonic laboratory data recorded to characterize the velocity and attenuation factor of a lava sample collected on the Vesuvius volcano.

The experimental set-up and processing developed in this study show that waveform inversion methods provide a useful tool for analysis of rock properties in laboratory experiments (Saracco *et al.* 2000).

ACKNOWLEDGMENTS

This work has been funded by the European Commission in the framework of the JOULE-THERMIE programme ERB4001GT972624, by the ACI ‘*Catastrophes Naturelles*’ of the CNRS, and by INSU/PNRN (Aléa sismique). The authors thank D. Gibert and F. Conil for the experimental set-up and T. Vanorio and J.-X. Dessa for interesting discussions. We are grateful to C. Wibberley for his English proofreading. Publication number 646 of Géosciences-Azur.

REFERENCES

- Aki, K. & Richards, P., 1980. *Quantitative Seismology: Theory and Methods*, W. H. Freeman, San Francisco.
- Chang, H. & McMechan, G., 1996. Numerical simulation of multi-parameter seismic scattering, *Bull. seism. Soc. Am.*, **86**, 1820–1829.
- Dessa, J.-X. & Pascal, G., 2003. Combined travelt ime and frequency-domain seismic waveform inversion: a case study on multi-offset ultrasonic data, *Geophys. J. Int.*, **154**, 117–133.
- Forgues, E., 1996. Inversion linéarisée multi-paramètres via la théorie des rais, *PhD thesis*, Institut Français du Pétrole–Institut de Physique du Globe, Paris.

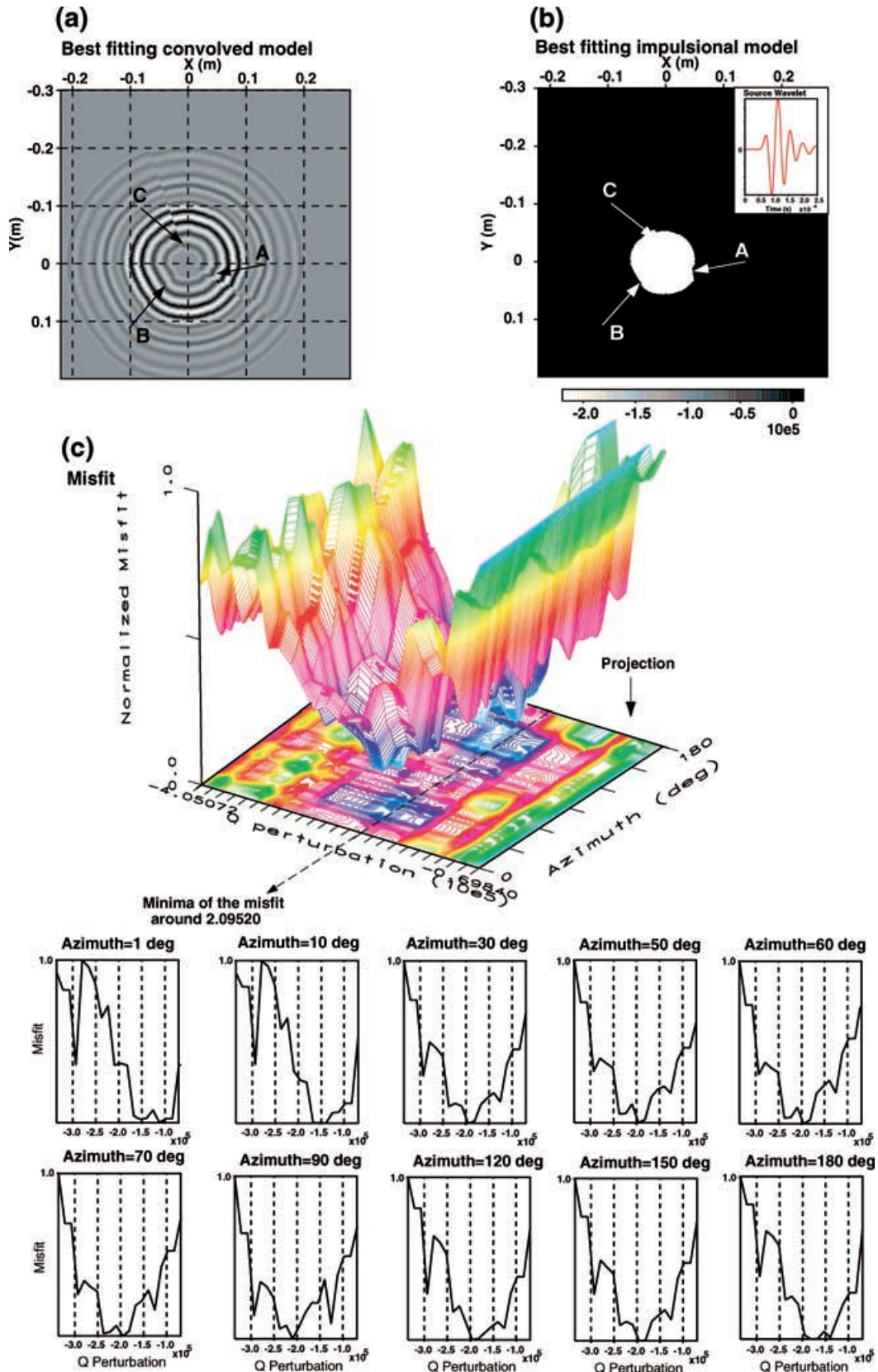


Figure 14. Results of the post-processing sequence in order to estimate δQ perturbation of the lava sample. (a) The best fitting convolved model for Q -factor and (b) the best fitting impulsive models for Q . The source wavelet used during the convolution processing is shown in the inset. A 3-D view of the misfit versus Q perturbation and azimuth in (c). On the bottom some azimuths is selected. The misfit presents a minimum around $\delta Q = 2.09520 \times 10^5$ and for some azimuths (i.e. 1° , 10° and $(160^\circ, 180^\circ)$) the attenuation perturbation is overestimated. This result is probably associated with the recovered discontinuities labelled A, B, C.

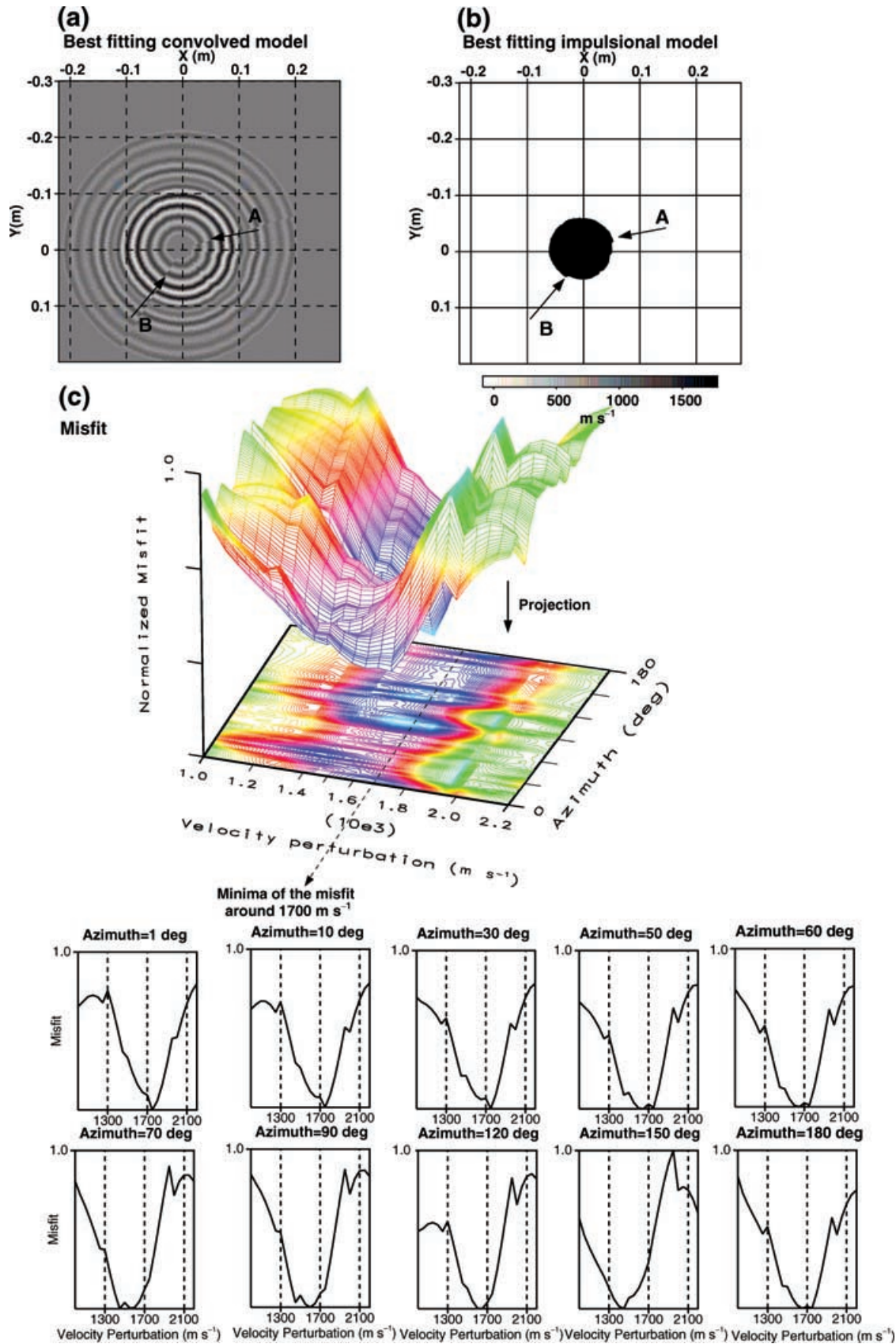


Figure 15. Results of the post-processing sequence in order to estimate δv perturbation of the lava sample. (a) The best fitting convolved model for v factor and (b) the best fitting impulse models for v . A 3-D view of the misfit versus Q perturbation for all the azimuths in (c). Minima are clearly identified for velocity $v = v_0 + 1700 \approx 3200 \text{ m s}^{-1}$ for the lava sample. Only for the azimuths around 30° and 150° is the velocity underestimated.

- Fujii, K. & Masui, R., 1993. Accurate measurements of the sound velocity in pure water by combining a coherent phase-detection technique and a variable path-length interferometer, *J. acoust. Soc. Am.*, **93**, 273–282.
- Gaffet, S., 1995. Teleseismic waveform modelling including geometrical effects of superficial geological structures near to seismic sources, *Bull. seism. Soc. Am.*, **85**, 1068–1079.
- Gaffet, S. & Bouchon, B., 1989. Effects of two-dimensional topographies using the discrete wavenumber boundary integral equation method in P-SV cases, *J. acoust. Soc. Am.*, **85**, 2277–2283.
- Jin, S., Madariaga, R., Virieux, J. & Lambaré, G., 1992. Two-dimensional asymptotic iterative elastic inversion, *Geophys. J. Int.*, **108**, 575–588.
- Lambaré, G., 1991. Inversion linéarisée de données de sismique réflexion par une méthode quasi-newtonienne, *PhD thesis*, Université de Paris VII., Paris.
- Lambaré, G., Virieux, J., Jin, S. & Madariaga, R., 1992. Iterative asymptotic inversion in the acoustic approximation, *Geophysics*, **57**, 1138–1154.
- Lomax, A., Zollo, A., Capuano, P. & Virieux, J., 2001. Precise, absolute earthquake location under Somma-Vesuvius volcano using a new three-dimensional velocity model, *Geophys. J. Int.*, **146**, 313–331.
- Ribodetti, A., Virieux, J. & Durand, S., 1995. Asymptotic theory for viscoacoustic seismic imaging, in *65th Annual International Meeting, Society of Exploration Geophysicists*, pp. 631–634, Society of Exploration Geophysicists, Tulsa, OK.
- Ribodetti, A. & Virieux, J., 1998. Asymptotic theory for imaging the attenuation factor Q, *Geophysics*, **63**, 1767–1778.
- Ribodetti, A., 1998. Imagerie sismique haute résolution pour les milieux dissipatifs, *PhD thesis*, Université de Nice.
- Ribodetti, A., Operto, S., Virieux, J., Lambaré, G., Valero, H.P. & Gibert, D., 2000. Asymptotic viscoacoustic diffraction tomography of ultrasonic laboratory data: a tool for rock properties analysis, *Geophys. J. Int.*, **140**, 324–340.
- Saracco, G., Ribodetti, A., Turquety, S. & Conil, F., 2000. Ultrasonic seismic imaging of lava samples by viscoacoustic asymptotic waveform inversion: calibration and developments, *IEEE Instrumentation and Measurement Technology Conference*, Extended Abstracts, **1**, 380–385.
- Sheriff, R., 1975. Factors affecting seismic amplitudes, *Geophys. Prospect.*, **23**, 125–138.
- Tarantola, A., 1987. *Inverse Problem Theory: Methods for Data Fitting and Model Parameter Estimation*, p. 613, Elsevier, Amsterdam.
- Thierry, P., Lambaré, G., Podvin, P. & Noble, M., 1999a. 3-D preserved amplitude prestack depth migration on a workstation, *Geophysics*, **64**, 222–229.
- Thierry, P., Operto, S. & Lambaré, G., 1999b. Fast 2D ray-Born inversion/migration in complex media, *Geophysics*, **64**, 162–181.
- Thierry, P., 1997. Migration/inversion 3-D en profondeur à amplitude préservée: application aux données de sismique réflexion avant sommation, *PhD thesis*, Université de Paris VII., Paris.
- Toksöz, M. & Johnston, D., 1981. *Seismic Wave Attenuation*, Society of Exploration Geophysicists Geophysics Reprint Series 2, p. 459, Society of Exploration Geophysicists, Tulsa, OK.
- Vanorio, T., Prasad, M., Patella, D. & Nur, A., 2002. Ultrasonic velocity measurements in volcanic rocks: correlation with microtexture, *Geophys. J. Int.*, **149**, 22–36.
- Valero, H.P., 1997. Endoscopie sismique, *PhD thesis*, Institut de Physique du Globe de Paris.
- Zamora, M., Sartoris, G. & Chelini, W., 1994. Laboratory measurements of ultrasonic wave velocities in rocks from the Campi Flegrei volcanic system and their relation to other field data, *J. geophys. Res.*, **99**, 13 553–13 561.
- Zollo, A., Marzocchi, W., Capuano, P., Lomax, A. & Ianaccone, G., 2002a. Space and time behaviour of seismic activity at Mt Vesuvius volcano, southern Italy, *Bull. seism. Soc. Am.*, **92**, 625–640.
- Zollo, A., D’Auria, L., De Matteis, R., Herrero, A., Virieux, J. & Gasparini, P., 2002b. Bayesian estimation of 2-D P-velocity models from active seismic arrival time data: imaging of shallow structure of Mt Vesuvius (southern Italy), *Geophys. J. Int.*, **151**, 566–582.